

ATMOSPHERIC FATE OF METHYL VINYL KETONE: PEROXY RADICAL REACTIONS WITH NO AND HO₂

Praske, E., J. D. Crouse, K. H. Bates, T. Kurtén, H. G. Kjaergaard, and P. O. Wennberg (2015). “Atmospheric fate of methyl vinyl ketone: Peroxy radical reactions with NO and HO₂”. In: *J. Phys. Chem. A* 119.19, pp. 4562–4572. DOI: 10.1021/jp5107058.

Abstract

First generation product yields from the OH-initiated oxidation of methyl vinyl ketone (3-buten-2-one, MVK) under both low and high NO conditions are reported. In the low NO chemistry, three distinct reaction channels are identified leading to the formation of (1) OH, glycolaldehyde, and acetyl peroxy R2a, (2) a hydroperoxide R2b, and (3) an α -diketone R2c. The α -diketone likely results from HO_x-neutral chemistry previously only known to occur in reactions of HO₂ with halogenated peroxy radicals. Quantum chemical calculations demonstrate that all channels are kinetically accessible at 298 K. In the high NO chemistry, glycolaldehyde is produced with a yield of $74 \pm 6.0\%$. Two alkyl nitrates are formed with a combined yield of $4.0 \pm 0.6\%$. We revise a three-dimensional chemical transport model to assess what impact these modifications in the MVK mechanism have on simulations of atmospheric oxidative chemistry. The calculated OH mixing ratio over the Amazon increases by 6%, suggesting that the low NO chemistry makes a non-negligible contribution toward sustaining the atmospheric radical pool.

B.1 Introduction

MVK is one of the most abundant oxygenated volatile organic compounds in the Earth’s atmosphere. It is a major product of the gas-phase oxidation of isoprene, a compound emitted by terrestrial vegetation to the atmosphere at a rate of approximately 500 Tg y⁻¹ (Guenther *et al.*, 2012). Oxidation of isoprene by the hydroxyl radical (OH) produces MVK with a yield that depends on the concentrations of NO and HO₂ and temperature. MVK is also produced during the oxidation of isoprene by ozone and has been quantified in car exhaust (Biesenthal and Shepson, 1997; Zhang and Zhang, 2002). Globally, approximately 100 Tg of MVK are produced

annually from isoprene according to the GEOS-Chem simulations described here (Bey *et al.*, 2001).

MVK has an atmospheric lifetime of approximately 10 h with respect to oxidation by OH ($[OH] = 1.5 \times 10^6$ molecules cm^{-3}), which constitutes its principal atmospheric loss process (Atkinson *et al.*, 2006). OH adds to either of the two olefinic carbon atoms forming distinct alkyl radicals. In the atmosphere, these alkyl radicals rapidly react with O_2 forming peroxy radicals (RO_2):



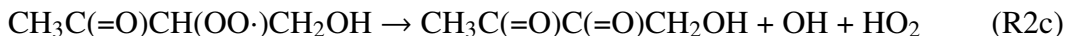
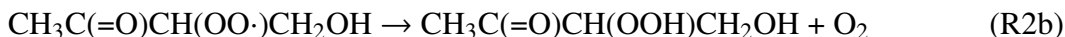
Tuazon and Atkinson (1989) studied the OH-initiated MVK oxidation in the gas phase and determined that R1a accounts for $72 \pm 21\%$ of the OH reactivity with the remaining following pathway R1b. The dominant fate of RO_2 radicals in the atmosphere is reaction with either HO_2 or NO. The reaction of MVK-derived RO_2 and NO to produce NO_2 , HO_2 , and carbonyl products has been previously characterized. Glycolaldehyde, methylglyoxal, formaldehyde, and peroxyacetyl nitrate have all been quantified as the primary first generation products of MVK oxidation under conditions where reaction with NO dominates the RO_2 fate (Galloway *et al.*, 2011; Tuazon and Atkinson, 1989). The yields of glycolaldehyde and methylglyoxal through NO-mediated chemistry were determined to be $64 \pm 8\%$ and $25 \pm 4\%$, respectively (Tuazon and Atkinson, 1989). The yield of organic nitrates has been estimated to be $10 \pm 10\%$ (Chuong and Stevens, 2004). Alkyl nitrates are of interest due to their interactions with aerosol as well as their ability to act as temporary reservoirs of NO_x , which can be transported and lead to ozone formation downwind (Perring *et al.*, 2013).

The primary focus of this study is the chemistry of the reaction of the RO_2 radicals formed in R1a and R1b with HO_2 . This chemistry is notably distinct, given the diverse set of reactions that $\text{RO}_2 + \text{HO}_2$ may undergo (Orlando and Tyndall, 2012). Traditionally, these reactions have been viewed as sinks for atmospheric radicals through the formation of organic hydroperoxides (Seinfeld and Pandis, 2006). As demonstrated here, however, this chemistry is largely HO_x neutral in the case of MVK. Two reaction channels R2a-R2b, previously described for the reaction of acetyl RO_2 and HO_2 (Dillon and Crowley, 2008; Hasson *et al.*, 2005, 2004; Jenkin *et al.*, 2008), are observed to occur for MVK RO_2 with substantial yields. We have also identified a carbonyl forming channel R2c, which has only been reported in the reactions of halogenated RO_2 with HO_2 (Hou *et al.*, 2005a,b; Hou and Wang,

expt #	objective	[MVK] ₀ (ppbv)	oxidant (ppmv)	[NO] ₀ (ppmv)	temp. (±2 K)	UV (%)
1	RO ₂ + HO ₂	85	H ₂ O ₂ , 2.5	-	296	100
2	RO ₂ + HO ₂	79	H ₂ O ₂ , 2.5	-	296	100
3	RO ₂ + HO ₂	62	H ₂ O ₂ , 2.5	-	296	100
4	RO ₂ + HO ₂ , hot	95	H ₂ O ₂ , 2.5	-	323	100
5	RO ₂ + HO ₂ , slow, hot	60	CH ₃ ONO, 0.050	-	323	12.5
6	RO ₂ + HO ₂ , slow, hot	28	H ₂ O ₂ , 1.6	-	323	12.5
7	RO ₂ + NO	75	CH ₃ ONO, 0.100	1.3	296	25
8	RO ₂ + NO	440	H ₂ O ₂ , 2.5	1.2	296	100
9	RO ₂ + NO, hot	75	CH ₃ ONO, 0.100	1.2	323	25
10	RO ₂ + NO, hot	78	CH ₃ ONO, 0.100	1.2	323	25

Table B.1: List of photo-oxidation experiments performed. For the UV lights, $J_{NO_2} = 2.5 \times 10^{-3} \text{ s}^{-1}$ at 100% illumination.

2005). The reaction pathways are shown below:



The discovery of efficient HO_x recycling in MVK chemistry adds to the growing number of new findings that the oxidation of isoprene and other biogenic alkenes in low NO environments is less HO_x consuming than previously understood (Crouse *et al.*, 2012, 2011; Peeters *et al.*, 2009; Surratt, 2013). Here, we use the GEOS-Chem atmospheric chemical transport model to evaluate the impact of this chemistry on simulated OH levels within the lower atmosphere.

B.2 Experimental Methods

We performed a series of photo-oxidation experiments in a small Teflon-walled chamber (Table B.1). Experiments were designed to evaluate the products of reactions of the peroxy radicals formed in R1a and R1b with both NO and HO₂. To evaluate the importance of unimolecular reactions of these peroxy radicals, we also investigated the dependence of the product distribution on peroxy radical lifetime and temperature.

B.2.1 Chemicals

Methyl vinyl ketone (99%, Sigma-Aldrich), 3-hydroxy-2-butanone (≥96%, Sigma-Aldrich), 4-hydroxy-2-butanone (95%, Sigma-Aldrich), glycolaldehyde dimer (Sigma-Aldrich), H₂O₂ (30% w/w, Macron), nitric oxide (1993 ± 20 ppmv NO in N₂,

Matheson), and isopropanol ($\geq 99\%$, Macron) were all used as purchased.

B.2.2 Chamber and Instruments

Experiments were carried out in a 1 m³ fluorinated ethylene propylene copolymer (Teflon-FEP, DuPont) environmental chamber at ambient laboratory pressure (~ 993 hPa), as previously described (Crouse *et al.*, 2011). The chamber was connected to instrumentation *via* ~ 2 m of 6.35 mm OD PFA tubing. Instrumentation included a Time of Flight Chemical ionization mass Spectrometer (ToF-CIMS), a triple quadrupole MS-MS CIMS, and a gas chromatograph with a flame ionization detector (GC-FID).

MVK was monitored by GC-FID, with product determination *via* CIMS. The GC-FID (Agilent 5890 II) had a run cycle of approximately 30 min and was equipped with a 30 m megabore 0.53 μm PLOT-Q column (JW Chemicals).

B.2.3 CIMS

The CIMS techniques have been previously described in detail (Crouse *et al.*, 2006; Paulot *et al.*, 2009b; St. Clair *et al.*, 2010). Reaction products were quantified using the CF_3O^- reagent ion ($m/z = 85$) at temporal resolution of 10 Hz. CF_3O^- was formed by passing 1 ppm of CF_3OOCF_3 in N_2 through a ^{210}Po radioactive source. The reagent ion was then introduced to a flow tube where the chamber sample was diluted (dry N_2 , 1675 standard cubic centimeters per minute). Due to clustering with the reagent ion, most masses reported here are represented as the sum of the nominal compound mass and m/z 85. Fluoride transfer can occur for acidic analytes. For example, nitric and acetic acids were detected primarily at m/z 82 and m/z 79, respectively. Observed ion signals were normalized to that of the reagent ion to account for variations in CF_3O^- fluence. The reagent ion was represented as the sum of $m/z = 86, 104,$ and 120 , which corresponds to $^{13}\text{CF}_3\text{O}^-$ and its cluster with water and H_2O_2 , respectively. Detection limits are typically ~ 10 pptv.

B.2.4 GC-CIMS

The CIMS was periodically connected to a GC column to enable the separation and quantification of isomers. The GC-CIMS technique has been previously described (Bates *et al.*, 2014; Lee *et al.*, 2014; Teng *et al.*, 2015). Briefly, both prior to and after photo-oxidation, samples of chamber air were analyzed using a gas chromatograph with the output of a 4 m Restek RTX-1701 column connected to the ToF-CIMS. The analytes were cryogenically trapped on the head of the column using an isopropanol

bath at approximately $-20\text{ }^{\circ}\text{C}$. Sample collection lasted 4 min to yield a total sample volume of about 150 cm^3 , after which a temperature ramp program was initiated ($30\text{ }^{\circ}\text{C}$ for 0.1 min, $+3\text{ }^{\circ}\text{C}/\text{min}$ until $60\text{ }^{\circ}\text{C}$, and $+10\text{ }^{\circ}\text{C}/\text{min}$ to $130\text{ }^{\circ}\text{C}$).

B.2.5 Calibration

Where available, synthetic standards were used to determine the sensitivity of the CIMS. For several of the products where standards were not available, we estimated the sensitivity using reagent ion-molecule collision rates, calculated using dipole moments and polarizabilities (see Section B.5) (Garden *et al.*, 2009; Su and Chesnavich, 1982). Isomer-specific sensitivities for the MVK-derived alkyl nitrates were previously determined by thermal dissociation LED-induced fluorescence coupled to the output of a GC column (Lee *et al.*, 2014). Glycolaldehyde, the principal MVK oxidation product upon which other yields are based, was calibrated using an authentic standard. Gas phase standards were prepared by methods involving either the evaporation of a solution containing glycolaldehyde or by decomposition of crystalline glycolaldehyde dimer. In the first method, a gravimetric standard of glycolaldehyde dimer was dissolved in methanol to yield a 2.8% w/w glycolaldehyde solution. A known quantity of this solution was injected *via* syringe into a sealed glass three-way vial, which was then transferred to the chamber by flushing with a known volume of dry zero air. In a second method, crystalline glycolaldehyde dimer was placed into a vial and heated to $100\text{ }^{\circ}\text{C}$ and vacuum purged to remove high volatility species as well as water and air. After 10 min, the vial was cooled to room temperature. A steady flow of dry N_2 transferred the headspace over the remaining glycolaldehyde dimer into a 50 L Teflon bag. Between the vial and the bag, a cold trap ($-15\text{ }^{\circ}\text{C}$) was used to reduce the transmission of dimer and other low volatility impurities. After the bag was filled, an aliquot was transferred into a glass sample cell and the absolute concentration of glycolaldehyde was determined by FTIR (Nicolet 560 Magna-IR) using tabulated absorption cross sections.(31) The referenced Pacific Northwest National Laboratory glycolaldehyde cross sections agree with those determined by Tuazon and Atkinson (1989) to better than 10%. A 500 cm^3 bulb was filled with the mixture and then flushed into the chamber with a known volume of air. The reproducibility of the calibration was verified twice for each technique, which confirmed that systematic and random error were below 7%. During each calibration, the signal on the chamber was monitored for 2-3 h in order to constrain wall loss processes and determine the effect of increasing relative humidity in the chamber. Over the time frame in which the sensitivity was derived,

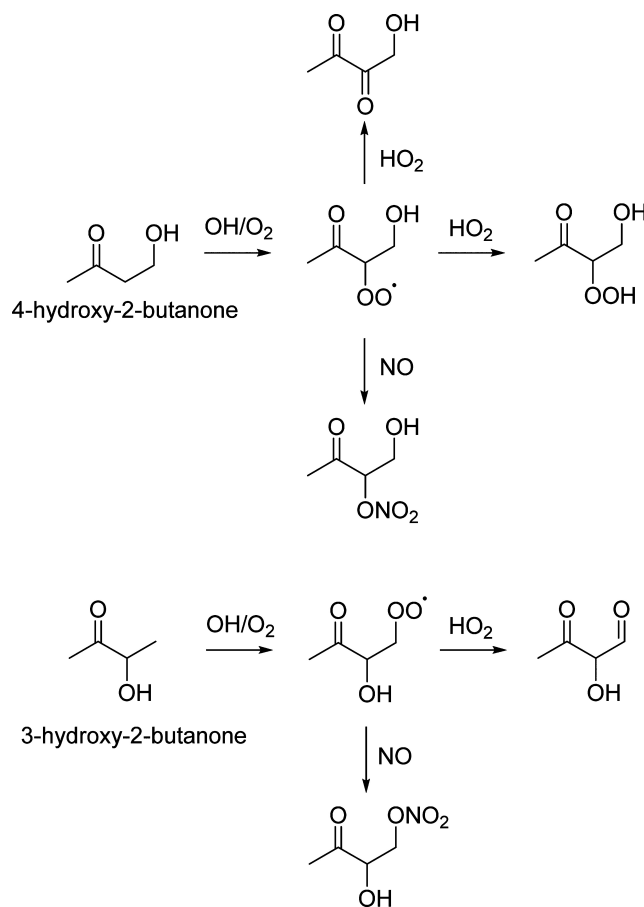


Figure B.1: Diagnostic experiments using commercially available precursors were conducted to identify structures associated with mass signals in MVK oxidation. The detected products resulting from NO/HO_2 reaction are shown.

the signal was stable to within $\pm 0.1\%$.

Standards for several of the proposed products of the oxidation of MVK are not commercially available. To identify these products, we synthesized several of the proposed compounds in the gas phase from commercially available precursors. 3-Hydroxy-2-butanone and 4-hydroxy-2-butanone were oxidized in the presence of H_2O_2 . Both compounds were first diluted in water to yield $\sim 10\%$ w/w solutions that were then volatilized into the chamber using the three-way glass vial addition method described above. The experiments (see Table B.2) were performed in both the HO_2 - and NO -dominated regimes. The oxidation products (see Figure B.1) were analyzed by GC-CIMS to compare retention times with those of the products of MVK oxidation.

expt #	objective	hydrocarbon	oxidant	NO added (ppmv)	OH scavenger
11	RO ₂ (R1a) + HO ₂	4-hydroxy-2-butanone	H ₂ O ₂	-	no
12	RO ₂ (R1a) + NO	4-hydroxy-2-butanone	H ₂ O ₂	0.8	no
13	RO ₂ (R1b) + HO ₂	3-hydroxy-2-butanone	H ₂ O ₂	-	no
14	RO ₂ (R1b) + NO	3-hydroxy-2-butanone	H ₂ O ₂	0.8	no
15	Photolysis	MVK	H ₂ O ₂	-	no
16	Photolysis	MVK	H ₂ O ₂	-	yes

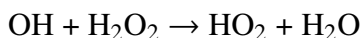
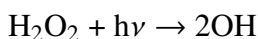
Table B.2: List of diagnostic experiments performed. Parentheses are used to indicate the isolation of peroxy radicals produced by reactions R1a or R1b.

B.2.6 MVK Photooxidation Experiments

The experiments performed are listed in Table B.1. Experiments were conducted at 296 ± 2 K, with the exception of experiments 4, 5, 6, 9, and 10 in which the chamber enclosure was heated and maintained at 323 K. Additions of MVK and oxidant were introduced sequentially to the chamber. MVK standards were prepared by serial dilution. First, a vapor pressure of ~ 13 hPa of MVK was siphoned into an evacuated 500 cm^3 glass bulb. An atmosphere of nitrogen was added to the bulb, which was subsequently pumped to ~ 13 hPa before being refilled with N₂. All pressures were measured by an MKS Baratron. The resulting MVK mixing ratio (~ 100 ppm) was verified by FTIR using tabulated absorption cross sections (Sharpe *et al.*, 2004). The sample was then introduced to the chamber and diluted with a regulated flow (20 L min^{-1} , MKS mass flow controller) of dry zero air.

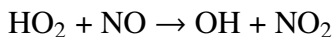
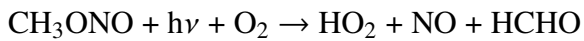
H₂O₂ was used as a HO_x precursor in some experiments, while CH₃ONO was used in others. A known amount (~ 8 mg) of H₂O₂ (30% w/w in water) was transferred into a three-way glass vial and evaporated into the chamber using a stream of dry zero air for about 20 min to yield 2.50 ± 0.25 ppm of H₂O₂. The residual mass of the vial was measured to ensure complete transfer of the contents to the chamber.

OH and HO₂ are produced *via* the photolysis of H₂O₂ under full chamber UV lights (8 Sylvania 350 blacklights with $J_{\text{H}_2\text{O}_2} \sim 1.7 \times 10^{-6} \text{ s}^{-1}$, $J_{\text{NO}_2} \sim 2.5 \times 10^{-3} \text{ s}^{-1}$, and $J_{\text{glycolaldehyde}} \sim 1.5 \times 10^{-6} \text{ s}^{-1}$):



CH₃ONO was used as a radical precursor to create conditions where the peroxy radicals react at approximately equal rates with HO₂ and NO. Methyl nitrite was synthesized using a procedure similar to that outlined in Taylor *et al.* (1980). A

known pressure of CH₃ONO was added to a 500 cm³ glass bulb, following a method similar to the addition of MVK. Only 2 UV lights were used in these experiments because the photolysis rate of CH₃ONO is much greater than that of H₂O₂ for the radiation emitted by our chamber lights. Radical generation proceeds by



For experiments designed to measure the alkyl nitrate yield (7, 8, 9, and 10), ~1 ppm of NO was added to the chamber at the start of the experiments using the primary standard described above.

After filling the chamber with all reactants and diluting to the desired volume, background signals were quantified *via* direct (without chromatographic separation) and GC-CIMS sampling. UV lights were then switched on until the mixing ratio of MVK had decayed ~10%. This amount was chosen to minimize the influence of secondary reactions and other loss processes while producing quantifiable yields of products. The product yields reported here are derived from this initial oxidation period.

Experiments 5 and 6 were performed to probe unimolecular pathways in the mechanism. Similar to previous experiments detailing the oxidation of methacrolein described by Crouse *et al.* (2012) the peroxy radical lifetimes were extended by halving the concentration of both MVK and oxidant and employing very low light flux conditions. Additionally, the chamber was heated to 50 °C to increase the rate of any RO₂ isomerization processes.

Finally, experiments 15 and 16 were performed to measure the photolysis of the products of MVK oxidation. MVK was oxidized in the presence of H₂O₂ until a sufficient signal level was attained for the product compounds of interest. At this point, oxidation was halted by switching the lights off. Isopropanol, an OH scrubber, was added to the chamber *via* a 500 cm³ glass bulb to yield a ~50 ppm mixing ratio. According to evaluated gas phase kinetic data (Atkinson *et al.*, 2006), >99% of OH present or subsequently produced preferentially reacted with the scrubber under these conditions. The chamber was fully illuminated once again for ~10 h. Photolysis experiments were conducted both with (experiment 16) and without (experiment 15) the presence of the OH scavenger.

B.2.7 Quantum Chemical Methods

We employed theoretical calculations to evaluate the thermodynamics of the three proposed reaction pathways for the reaction of MVK-derived RO₂ and HO₂ R2a-R2c. The lowest energy conformer for each of the stationary points along the reaction was found using the systematic search in Spartan14 except for the transition states (TS) where the structures were inferred based on previous calculations in the literature (Hasson *et al.*, 2005; Hou *et al.*, 2005a,b; Hou and Wang, 2005). The B3LYP hybrid density functional with the standard 6-31+G(d) double- ζ basis set was used in these initial calculations. The optimized structure of each stationary point was subsequently refined with the the wB97XD functional (Chai and Head-Gordon, 2008) and the aug-cc-pVDZ and aug-cc-pVTZ, double and triple- ζ basis set, respectively (wB97XD/aVDZ and wB97XD/aVTZ). Only minor differences in structures are found between the wB97XD/aVDZ and wB97XD/aVTZ optimized structures. Harmonic vibrational frequencies are calculated for both wB97XD methods to confirm that each structure is either a minimum or a transition state (one imaginary frequency). The transition state (TS) structures are shown to connect the reactant or reactant intermediate and product on either side *via* intrinsic reaction coordinate (IRC) calculations with the wB97XD/aVDZ method. For all calculations, we used the unrestricted Kohn-Sham formalism with the spin symmetry of the initial guess wave function broken (Guess = Mix). The wB97XD DFT calculations are calculated using the Gaussian09 program suite with the default convergence criteria (Frisch *et al.*, 2009).

We improved the accuracy of the thermochemistry by calculating single-point energies with the explicitly correlated CCSD(T)-F12a/VDZ-F12 method (F12) at the wB97XD/aug-cc-pVTZ optimized structures (Knizia *et al.*, 2009). The F12 calculations on open-shell species are restricted open coupled cluster [ROCCSD(T)-F12] calculations based on a restricted-open Hartree-Fock (ROHF) determinant. The T1 diagnostic is less than 0.034 in all F12 calculations, which indicates that multiconfiguration effects are limited. All the F12 coupled cluster calculations are performed using the MOLPRO₂₀₁₀ program suite with the default convergence criteria (Werner *et al.*, 2012).

We obtain ΔG for each structure with the F12 energies and the thermal contribution from the wB97XD/aug-cc-pVTZ calculation.

regime	RO ₂ + NO	RO ₂ + HO ₂
Y_{GLYC}	$74 \pm 6.0\%$	$38 \pm 4.6\%$
Y_{MGLY}	$24.12 \pm 0.14\%^a$	$4 \pm 1\%^b$
$Y_{\alpha-DK}$	-	$14 \pm 5.3\%$
Y_{HHP}	-	$27 \pm 9.7\%$
Y_{MVKN}	$2.4 \pm 0.4\%$	-
$Y_{MVKN'}$	$1.6 \pm 0.4\%$	-

Table B.3: Measured yields (Y) based on experiments 7 and 8 for the high-NO regime and experiments 1-3 for the RO₂ + HO₂ regime. Abbreviations are: GLYC = glycolaldehyde, MGLY = methylglyoxal, α -DK = C₄ α -diketone, HHP = C₄ 4,3 hydroxy hydroperoxide, MVKN = 3-ONO₂,4-OH-MVK, and MVKN' = 3-OH,4-ONO₂-MVK. Methylglyoxal was not measured in these experiments; values come from ^aGalloway *et al.* (2011) or ^bPersonal communication from F. N. Keutsch.

B.3 Results and Discussion

B.3.1 Product Yields

The product yields from the reaction of the hydroxy peroxy radicals formed *via* R1a and R1b with NO or HO₂ are shown in Table B.3. Example time traces of the decay of MVK and the growth of these products are shown in Figure B.2.

The yield of glycolaldehyde is computed from the rate of its formation divided by the loss rate of MVK. The yields of the other products are determined relative to glycolaldehyde. The tabulated uncertainty in the yield of glycolaldehyde includes error in its measurement and from error in the amount of MVK oxidized (due to uncertainty in the GC-FID measurements and in the initial concentration of MVK resulting from uncertainty in the infrared cross sections). The uncertainty in the yields of the other products includes error in the absolute yield of glycolaldehyde in addition to error in the slope of the linear regression of the relative rate of product formation. Uncertainty in the calibration of glycolaldehyde is $\sim 7\%$, and for the hydroxy nitrates is $\sim 12\%$. Calibration of the remaining compounds is significantly more uncertain (30%) due to the lack of authentic standards (see Table B.6 of the Supporting Information). The error bounds in Table B.3 also include uncertainty in both measured and calculated calibration factors. Due to uncertainty in the calibrations, the yields do not necessarily achieve carbon parity.

In direct sampling from the chamber, the signal from both hydroxy nitrate isomers produced from MVK, 4-hydroxy-3-nitrooxy-2-butanone (MVKN), and 4-nitrooxy-3-hydroxy-2-butanone (MVKN'), is measured as the cluster with CF₃O⁻ (m/z 234).

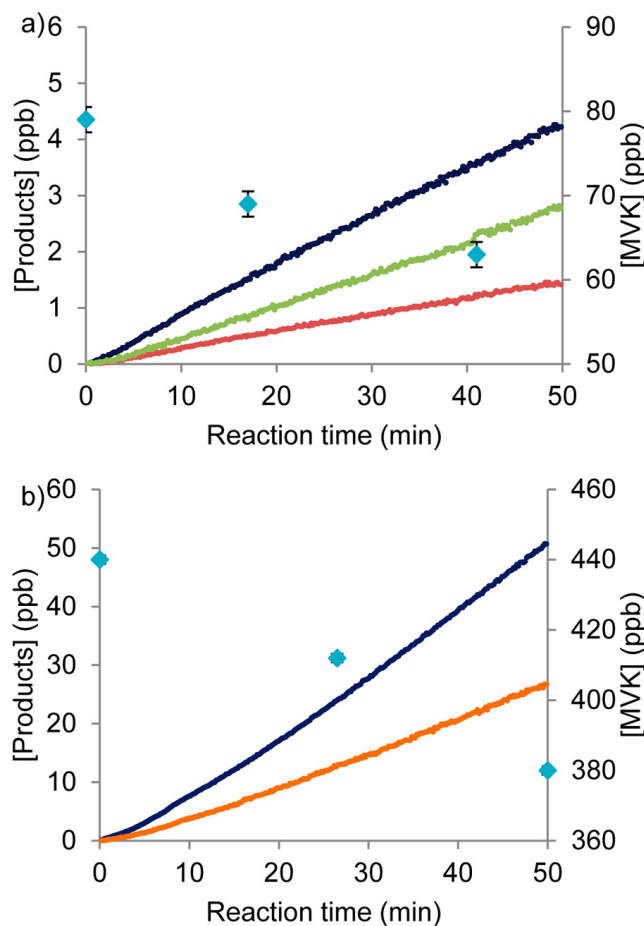


Figure B.2: Reaction profiles demonstrating the HO₂ and NO dependence of the chemistry. Species shown are glycolaldehyde (dark blue), a 4,3-hydroxy hydroperoxide (green), an α -diketone (red), organic nitrates ($\times 10$, orange), and MVK (light blue diamonds). Data are derived from (a) experiment 2 in the low NO regime and (b) experiment 8 in the high NO regime. Error bounds reflect the uncertainty in the GC-FID quantification of MVK.

The isomer-specific yields were determined using GC-CIMS. We assigned the chromatographic peaks by comparing the individual retention times with those of the hydroxy nitrate carbonyls produced in experiments 12 and 14 (Figure B.10 of the Supporting Information).

The yield and identification of the dicarbonyl compound was based on analysis of experiments 11, 13, 15, and 16. As discussed below, there are two possible compounds detected as a CF₃O⁻ cluster with C₄O₃H₆ at m/z 187: an α -diketone (1-hydroxy-2,3-butanedione) or an aldehyde (2-hydroxy-3-oxobutanal). However, the oxidation of 4-hydroxy-2-butanone in experiment 11 produced a yield of the m/z 187 compound relative to glycolaldehyde identical to that shown in Table B.3. On

the other hand, the m/z 187 signal observed from 3-hydroxy-2-butanone oxidation in experiment 13 was produced as a second-generation product and was not accompanied by coproduction of glycolaldehyde. Thus, we conclude that the observed m/z 187 signal primarily arises from the α -diketone and that the contribution of the aldehyde is likely small (<2%).

Only a single hydroxy hydroperoxide was observed in GC-CIMS chromatograms obtained following the low NO oxidation of MVK (experiments 1-3). The elution time of this compound matched that of the hydroperoxide formed in experiment 11. The hydroxy hydroperoxides produced in experiments 1-3 and 11 also share identical and characteristic ion chemistry. Three major product ions are observed: m/z 205 results from the cluster of CF_3O^- ; m/z 139 ($\text{F}\cdot\text{C}_4\text{H}_8\text{O}_4^-$) results from fluoride transfer; m/z 101 ($\text{C}_4\text{H}_5\text{O}_3^-$) likely results from loss of water and HF; and FCO_2^- (m/z 63) is a fragment of m/z 205 characteristic of CF_3O^- chemical ionization of hydroxy hydroperoxides (Paulot *et al.*, 2009b). The product ions (m/z 205:139:101:63) are produced in a ratio of 5:10:6.5:1. This analysis is further detailed in Figure B.10 of the Supporting Information. Given the identical elution time and similar product ion distribution between the MVK hydroperoxide and those derived from the oxidation of 4-hydroxy-2-butanone, we identify this hydroperoxide as 3-hydroperoxy-4-hydroxybutan-2-one (4,3-hydroxy hydroperoxide).

B.3.2 Reaction of RO_2 with NO: Constraining the Ratio R1a:R1b

In the reaction of the two peroxy radicals produced in R1a and R1b with NO, two alkoxy radicals and two alkyl nitrates are produced (see Figure B.3). Tuazon and Atkinson (1989) and Galloway *et al.* (2011) suggested that the internal and external alkoxy radicals decompose to glycolaldehyde and methylglyoxal with 100% yield, respectively. Consistent with this hypothesis, we have calculated the energy barriers associated with decomposition of the alkoxy formed from the reaction of the peroxy radical produced in R1a with NO. We find that fragmentation to methylglyoxal is likely uncompetitive with fragmentation to acetyl peroxy (PA) and glycolaldehyde (8.2 vs 1.5 kcal mol⁻¹ in electronic energy, see the Supporting Information). This is consistent with the structure-activity relationship of Vereecken and Peeters (2009), which suggests these barriers to be 8.1 versus 3.7 kcal mol⁻¹, respectively. Thus, the product yields shown in Table B.3 suggest that the branching to R1a, derived by adding the glycolaldehyde yield and that of the corresponding hydroxy nitrate, is $76 \pm 14\%$, while that to R1b is $24 \pm 14\%$. The branching of R1b is defined as the difference between unity and the branching to R1a. Our estimation of the

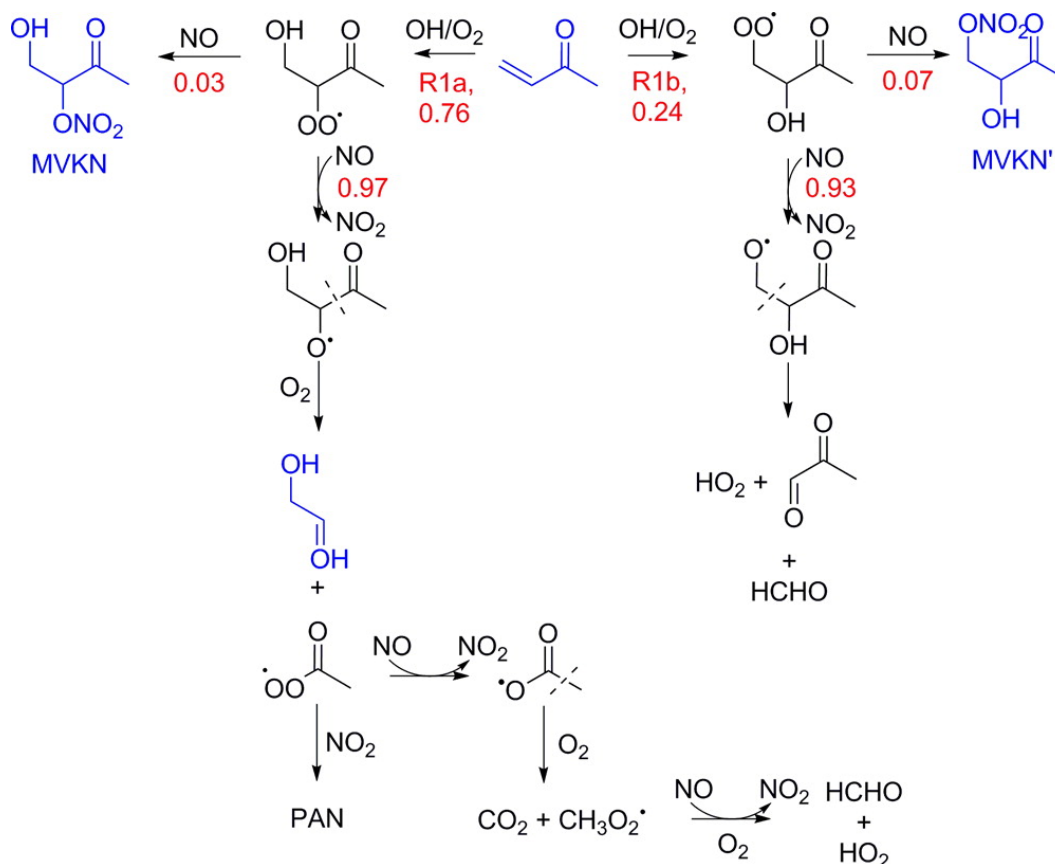


Figure B.3: Proposed mechanism for the high-NO regime (after Tuazon and Atkinson (1989)). Observed species are indicated in blue. Branching and yields (T = 296 K, P = 993 hPa) are in red.

branching ratio is consistent with previous estimates (Galloway *et al.*, 2011; Tuazon and Atkinson, 1989).

B.3.3 Reaction of RO₂ with NO: Formation of Alkyl Nitrates

The alkyl nitrate branching ratio from the reaction of the RO₂ produced in R1a with NO is $3.2 \pm 0.6\%$ at 296 K, while the branching ratio from the RO₂ produced in R1b is more than a factor of 2 larger ($6.6 \pm 1.5\%$). The combined yield at 296 K is $4.0 \pm 0.6\%$, much lower than previously suggested (Chuong and Stevens, 2004; Tuazon and Atkinson, 1989). Comparing the yields from experiments 7 and 8 with those of 9 and 10, we find that the combined yield is a factor of ~ 1.8 times lower at 323 K than at 296 K. Furthermore, at 323 K, the production ratio of MVKN to MVKN' is 1.10 ± 0.05 .

Alkyl nitrates likely form in a roaming radical mechanism. This mechanism

proceeds following destabilization of the ROONO moiety. In some cases, the nascent radicals do not separate but rather reform an activated RONO₂ complex, which then undergoes collisional stabilization to form the nitrate (Butkovskaya *et al.*, 2015; Dibble, 2008; Herath and Suits, 2011; O'Brien *et al.*, 1998). As such, the yield will depend on the lifetime of the complex. This general mechanism is consistent with findings that alkyl nitrate yields tend to increase with the size of molecule (Carter and Atkinson, 1989) and decrease with increasing temperature (Atkinson *et al.*, 1983). In addition, several studies have suggested that the formation of nitrates becomes less favorable when neighboring groups weaken the RO-ONO bond, enhancing the rate of decomposition (Matsunaga and Ziemann, 2009, 2010b; O'Brien *et al.*, 1998). Using the β -hydroxy nitrate yields quantified in our recent study of nitrates formed in the oxidation of alkenes (Teng *et al.*, 2015), we expect, based on the molecular size alone, that the alkyl nitrate yield from MVK would be ~14%. The much lower yield measured likely reflects destabilization of the RO-ONO moiety by the electron-withdrawing characteristics of the ketone group. Additionally, the lower yield and stronger temperature dependence of the nitrate formed from the RO₂ produced in R1a suggests that a β -ketone is more destabilizing than a γ -ketone.

The atmospheric fate of these nitrates remains unclear. A recent theoretical study has reported that the atmospheric lifetime of MVKN and MVKN' will be limited by photolysis (~5 h) (Müller *et al.*, 2014). Upon further oxidation by OH, the nitrates have been proposed to generate formic and pyruvic acid (Paulot *et al.*, 2009a).

B.3.4 Reaction of RO₂ with HO₂: New Chemistry and Radical Recycling

Reaction of the peroxy radicals with HO₂ is remarkably efficient in the recycling of radicals. We identified R2a-R2c for the reaction of HO₂ with the MVK RO₂ arising from R1a (see Figure B.4).

The large yield of glycolaldehyde (~40%) suggests that the OH radical is recycled efficiently *via* R2a. This chemistry is not unprecedented. Recent studies have demonstrated that OH generation occurs in several similar systems (Dillon and Crowley, 2008; Hasson *et al.*, 2005, 2004). For example, reaction of HO₂ with PA radical, produced in R2a upon addition of O₂ to the CH₃C(O) radical, has been shown to follow three pathways. The dominant channel (R3a, yield = 0.61 ± 0.09 (Gross *et al.*, 2014)) produces OH and acetoxy radicals, while peracetic acid (R3b) and acetic acid and O₃ (R3c) are produced in smaller yields (Dillon and Crowley, 2008; Hasson *et al.*, 2005, 2004, 2012; Jenkin *et al.*, 2007):

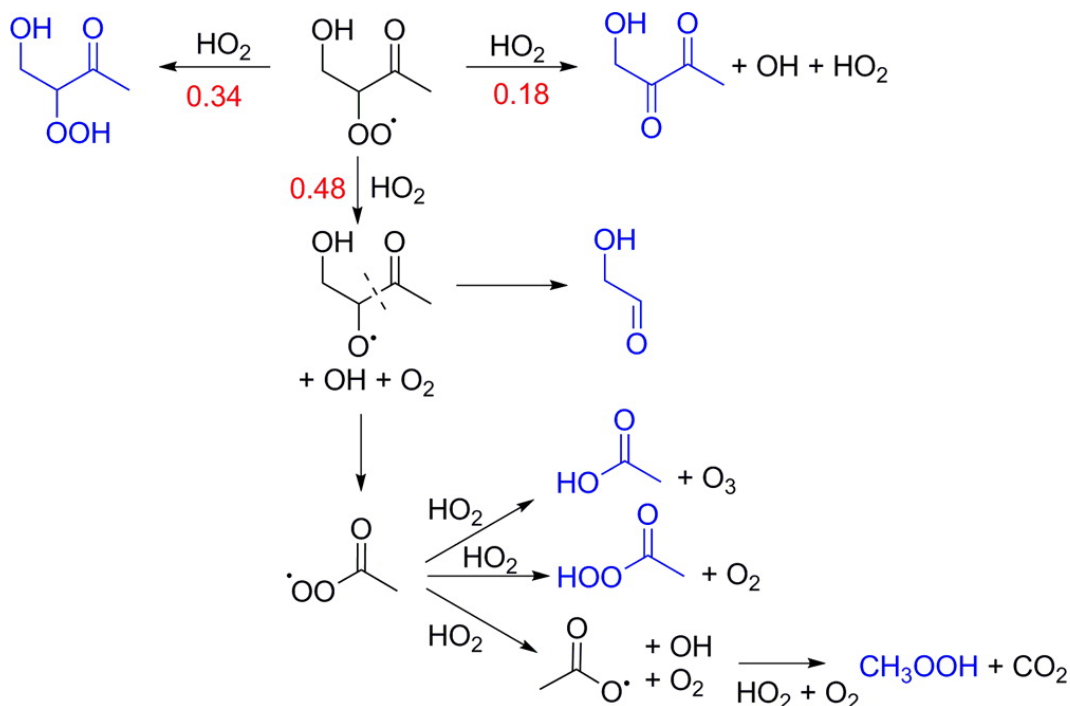
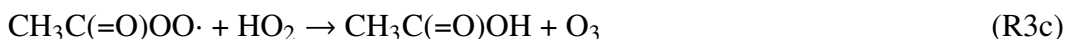
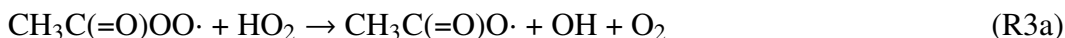


Figure B.4: Proposed mechanism for the OH-initiated oxidation of MVK following R1a in the HO₂-dominated regime. Observed products are indicated in blue. Yields (T = 296 K, P = 993 hPa) are in red.



In the presence of HO₂, the radical produced in R3a leads to formation of methyl hydroperoxide (MHP):



All stable organic end products identified in R3-R6 were detected in the HO₂-mediated reaction of MVK RO₂ and suggest greater radical recycling occurring beyond the initial OH reformation in R2a.

The 4,3-hydroxy hydroperoxide produced *via* R2b was found to promptly photolyze (Figure B.5). Independent of whether an OH scrubber was added (experiments 15 and 16), the hydroperoxide decayed with a first-order loss rate of $3.0 \pm 0.1 \times 10^{-5} \text{ s}^{-1}$. Scaling the J_{NO_2} in our chamber ($2.5 \times 10^{-3} \text{ s}^{-1}$) to that of a typical noontime atmosphere (0.01 s^{-1}) suggests that the atmospheric lifetime of

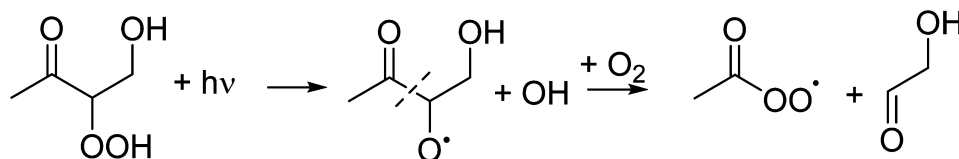


Figure B.5: Photolysis of the 4,3-hydroxy hydroperoxide, assuming cleavage of the O-OH bond, is expected to form PA and glycolaldehyde, and recycle OH. Rapid photolysis of this species was observed.

this hydroxy hydroperoxide is short ($\ll 1$ day). Assuming cleavage of the O-OH bond as the primary photolytic decomposition pathway, R2b will also recycle OH radicals efficiently.

The α -diketone produced *via* R2c likely results from a mechanism previously thought to be exclusive to halogenated RO₂. As we show below, this route likely produces OH + HO₂ in addition to the carbonyl. Similar chemistry was originally proposed by Wallington *et al.* (1994) to explain the formation of HC(=O)F in the reaction of CH₂FO₂ and HO₂. More recent theoretical studies have demonstrated that the energetic barrier to formation of OH and HO₂ from single-carbon fluorinated and chlorinated RO₂ is lower than the pathway to formation of H₂O and O₂, as originally proposed (Hou *et al.*, 2005a,b; Hou and Wang, 2005). To our knowledge, the MVK system provides the first evidence for this chemistry in nonhalogenated peroxy species.

Rapid photolysis has been previously reported for α -diketones (Bouzidi *et al.*, 2014). We designed experiments 15 and 16 to measure the rate of photolysis for the hydroxy diketone (m/z 187). Both prior to and after the initiation of photolysis, the signal was monitored for a period of 2 h to measure the wall loss rates. These were determined to be $2 \times 10^{-7} \text{ s}^{-1}$ and $2 \times 10^{-6} \text{ s}^{-1}$ before and after photolysis, respectively. Upon illumination by UV light, the m/z 187 signal decayed $\sim 20\%$ at a consistent rate. After 4 h, however, the loss ended such that an exponential decay no longer fit the data. This is likely due to the formation of a third-generation isobaric compound. Whether production of this compound existed during the initial period, although at a lower rate, is uncertain. Thus, we can only determine a loosely constrained value of $\sim 1 \times 10^{-5} \text{ s}^{-1}$, which includes corrections for wall loss and reaction with OH ($< 1\%$ due to the presence of an OH scrubber). This rate is lower than the calculated photolysis rate of a similar α -diketone, methylglyoxal, under similar conditions ($4.1 \times 10^{-5} \text{ s}^{-1}$).

B.3.5 Internal OH Addition

We are unable to identify the majority of the products of the reaction of HO₂ with the terminal RO₂ (formed *via* R1b). By reference to the reactions arising from external OH addition (R1a), the products are likely methylglyoxal, a hydroperoxide, and an aldehyde. The instruments employed in this study are insensitive to methylglyoxal, and thus we turn to unpublished data collected in the HO₂-dominated regime during the same set of experiments reported by Galloway *et al.* (2011). Preliminary analysis of this data *via* personal communication from the authors suggests an overall methylglyoxal yield of ~4%. In the current study, only a single *m/z* 205 peak, identified as the 4,3-hydroxy hydroperoxide, was observed in GC-CIMS analysis. No other peaks resembling a fragmentation pattern characteristic to hydroperoxide functionality were located in the vicinity of the elution time of the observed *m/z* 205 compound. It is possible that ionization of the 3,4-hydroxy hydroperoxide results in fragmentation to undetectable products. Alternatively, the hydroperoxide may decompose rapidly on the chamber walls. The C₄ aldehyde, as explained earlier, appears to be produced in, at most, a small yield. It may also be possible to form other products which are not observed by our CIMS.

B.3.6 Unimolecular RO₂ Channels

Functionalized peroxy radicals are known to undergo unimolecular hydrogen shifts from neighboring substituents (Crouse *et al.*, 2013; Orlando and Tyndall, 2012). Recent theoretical studies have suggested that a unimolecular pathway involving a 1,5 H-shift from the terminal hydroxy group to the RO₂ (R1a) could be of significance in the production of methylglyoxal and formaldehyde (see Figure B.6) (Asatryan *et al.*, 2010; Peeters *et al.*, 2009). While this mechanism proceeds through different intermediates, the end products are likely identical to the pathway involving HO₂ reaction with the terminal RO₂ to produce RO. Thus, the detection of this mechanism is complicated. Experiments 5 and 6 were designed to promote isomerization processes through active heating of the chamber to 50 °C and extension of RO₂ lifetimes. The product distributions and yields observed in these experiments were very similar to those seen in experiments 1-3. While the majority of products arising from R1b are poorly characterized, the ratio of MVKN to MVKN' in experiment 5 was consistent with those obtained in experiments 9 and 10. This suggests that neither of the RO₂ radicals had a significant unimolecular channel under the experimental conditions probed here.

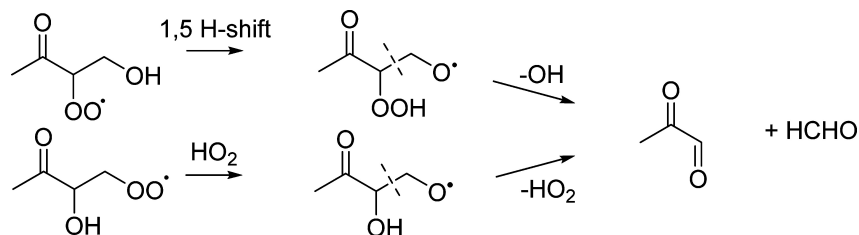


Figure B.6: A 1,5 H-shift, as suggested by Peeters *et al.* (2009) and Asatryan *et al.* (2010), is difficult to detect by the end products alone, as two pathways exist to their formation.

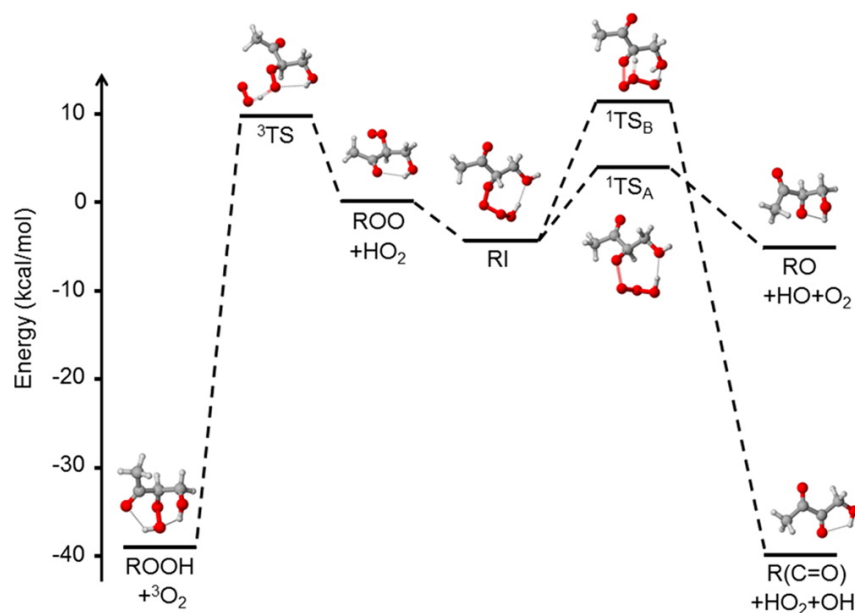


Figure B.7: Relative energies (ΔG_{298K}) for the three $RO_2 + HO_2$ channels. We have used wB97XD/aug-cc-pVTZ thermochemistry with ROHF-ROCCSD(T)-F12/VDZ-F12 energies. The wB97XD/aug-cc-pVTZ geometries for each of the stationary points are shown.

B.3.7 Quantum Chemical Calculations

Figure B.7 and Table B.4 show that all three postulated reaction pathways R2a-R2c in the reaction of HO_2 with RO_2 R1a are kinetically accessible at 298 K. Transition states for the reactions leading to the hydroperoxide (ROOH) and the alkoxy (RO) corresponded to those found for acetylonyl RO_2 in the literature (Hasson *et al.*, 2005). In addition, a new channel leading to a diketone [$R(C=O)$] has been found. For all but TS_A of the reaction leading to RO, there is no significant spin contamination observed, with $\langle S^2 \rangle$ being within 0.02 of the expected values for singlet (0), doublet (3/4), and triplet (2), respectively (see Table B.9 of the Supporting Information).

	ΔE^a	ΔE^b	ΔG^c	TS (imaginary frequency, cm^{-1})
ROO + HO ₂	0.0	0.0	0.0	-
³ TS	-3.2	+0.7	+10.2	934i
ROOH + O ₂	-39.2	-43.1	-38.9	-
RI	-12.2	-20.4	-4.1	-
¹ TS _A	2.5	-8.3	+4.1	212i
RO + OH + O ₂	+5.7	+8.1	-5.0	-
¹ TS _B	11.2	-0.7	+12.0	905i
R(C=O) + OH + HO ₂	-22.3	-26.2	-40.0	-

Table B.4: Energetics of the different RO₂ + HO₂ channels. Energies are in units of kcal mol⁻¹ and are calculated with ^awB97XD/aug-cc-pVTZ, ^bROHF-ROCCSD(T)-F12/VDZ-F12//wB97XD/aug-cc-pVTZ, and ^cthe wB97XD/aug-cc-pVTZ thermochemistry with CCSD(T)-F12/VDZ-F12 single-point energy correction.

The ROOH reaction producing ground state O₂ takes place on the triplet surface *via* the transition state ³TS (almost iso-energetic with the reactants) with a moderate free-energy barrier of about 10 kcal mol⁻¹. Tunneling will slightly enhance the reaction rate along this surface by a factor similar to that of the R(C=O) channel.

The RO reaction occurs *via* a tetroxide intermediate (labeled RI) and a low-energy, open-shell singlet transition state TS_A with a free-energy barrier of about 4 kcal mol⁻¹. The immediate products of TS_A are RO and an HO₃ radical, which further decomposes to OH and O₂. The structure and stability of HO₃ is a challenging problem for quantum chemical methods. Even high level methods such as CCSD(T)-F12 do not describe it accurately (see Zhou *et al.* (2013), Varandas (2012), and references therein).

We have also identified a reaction path leading to the α -diketone [R(C=O)]. This channel also proceeds *via* the tetroxide intermediate RI but to TS_B with a free-energy barrier of about 12 kcal mol⁻¹ and leads to the diketone and an H₂O₃ radical; the latter decomposes to OH + HO₂. Decomposition to H₂O and triplet O₂ would be even more energetically favorable but is spin-forbidden as the reaction takes place along the singlet potential energy surface.

We have also found an alternative tetroxide structure about 2 kcal mol⁻¹ below RI in electronic and free energy. This tetroxide can also decompose to both RO and R(C=O) products, although through a higher energy TS than the ones shown in Figure B.7. The two tetroxides differ only in their H-bonding pattern (see the Supporting Information).

We were unable to locate a transition state between the free reactants and either of the tetroxides, and we thus assume they form without a significant energy barrier.

The free-energy barriers computed for the three reaction routes, as shown in Table B.4, are within a few kcal mol⁻¹ of each other. The electronic energy of all the transition states is around or below the electronic energy of the reactants. Furthermore, the routes with the largest free-energy barrier (leading to R(C=O) and ROOH) are slightly assisted by tunneling. The effect of tunneling with the Eckart tunneling correction was calculated to be a factor of 3 for the diketone channel and insignificant for the RO channel (Eckart, 1930).

The uncertainty of the computed energy barriers is possibly higher than the usual few kcal mol⁻¹ for CCSD(T)-F12/VDZ-F12 energies due to the spin issues in particular for TS_A and multireference issues (see the discussion of the HO₃ intermediate product above; see also Section B.5). Thus, quantitative predictions of product yields are not reliable. Qualitatively, however, the calculations are consistent with the experimental observations, with the highest yields observed for the RO channel, followed by the ROOH and R(C=O) channels.

B.3.8 Atmospheric Implications

To assess the importance of the chemistry described here, we employed GEOS-Chem, a widely used chemical transport model (Bey *et al.*, 2001). A 1 year simulation (January to December 2012) of the model was conducted on a global 4° latitude × 5° longitude grid. The alkyl nitrate yield reported in this work was incorporated into the base chemistry to isolate the impact of HO₂ chemistry. Changes to the mechanism were applied separately to the base model to evaluate the impact of each modification of the chemistry. We began by implementing the yields of first generation products described by R2a-R2c (MVK scenario). An additional scenario (MVK + RCO₃) was created to assess the impact of PA radical production through R2a. The default GEOS-Chem 2012 mechanism does not treat PA according to recent findings. Thus, the most recent measurement of the OH yield from the reaction of PA + HO₂ was incorporated into both the base and the revised mechanism so as not to bias the results (Gross *et al.*, 2014). Given the considerable yield of PA in R2a, we believe this scenario to be most representative of the findings reported in this work. In order to provide an external benchmark, the OH production resulting from methacrolein (MACR) isomerization was included in a separate run (Crouse *et al.*, 2012). The final simulation incorporated all revisions

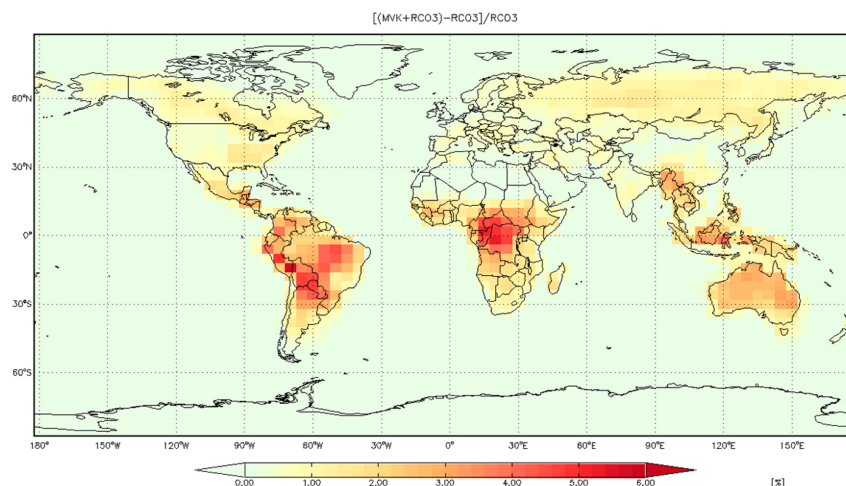


Figure B.8: Annual-averaged OH mixing ratio difference for 2012 resulting from the revised MVK mechanism (MVK + RCO₃). Results are reported for 0-1 km above the surface.

scenario	OH (ppt)	increase over base (%)
base	0.0539	0.00
MVK	0.0541	0.30
MVK + RCO ₃	0.0544	0.89
MACR	0.0541	0.35
all + J _{ROOH}	0.0547	1.33

Table B.5: Comparison of various model scenarios with the increase determined relative to the base chemistry (see Section B.5 for scenario definitions). Global annual mean OH values were determined by averaging over all space between 0 and 1 km above the surface.

of the previous scenarios and the fast photolysis of MVK ROOH. We find these changes result in a greater than 1% increase in the global mean boundary layer concentration of OH (Table B.5). Locally, the impact is larger. In the forested tropical boundary layer, simulated OH concentrations are up to 6% larger (Figure B.8).

B.4 Conclusions

HO_x recycling channels have been proposed to explain first generation products arising from the oxidation of isoprene in pristine environments (Crouse *et al.*, 2011; Peeters *et al.*, 2009), as well as the production of hydroxyacetone from MVK's atmospheric sister compound, methacrolein (Crouse *et al.*, 2012). Yet the atmospheric chemistry of MVK, particularly in environments with low concentrations of NO, has

been largely unexplored. Here we demonstrate a number of new radical recycling channels that contribute to sustaining the oxidizing capacity of the atmosphere. We further illustrate dicarbonyl formation in a novel mechanism previously identified only for halogenated peroxy species. This finding suggests that carbonyl products may arise from reaction of HO_2 with other substituted peroxy radicals in an overall HO_x neutral process.

B.5 Supporting Information

B.5.1 Instrumental Calibration

CIMS sensitivity factors are determined by the specific molecule-ion collision rates and the binding energy of the resulting clusters. The rate of collision can be estimated from the dipole moment and polarizability of the analyte (Su and Chesnavich, 1982). These properties were calculated using DFT for the C₄ compounds produced in the oxidation of MVK. Because the dipole moment depends on the structural conformation of the molecule, we calculate the population density and dipole of all conformers with a relative population of >5% at 298 K to estimate the conformationally-weighted property. The polarizability was not found to exhibit significant conformational dependence and the calculation was therefore based on the lowest energy structure. Further detail of similar calculations is provided by Garden *et al.* (2009) A summary of these properties along with calibration factors for MVK systems is shown in Table B.6 in the Supporting Information.

B.5.2 Chemical Transport Model

Tables B.7 and B.8 in the Supporting Information describe changes made to the GEOS-Chem mechanism (Bey *et al.*, 2001). The maps (Figures B.11, B.12, and B.13 in the Supporting Information) illustrate the output of the model resulting from the changes. These simulations employ GEOS-Chem v9-02 using GEOS5 meteorology and initialize the model with a 1.5 year spinup before the January-December 2012 final simulation. The Rosenbrock Rodas-3 with Kinetic PreProcessing software was used as the solver.

B.5.3 Quantum Chemical Calculations

To test whether using a UHF reference wave function would lower the coupled-cluster energies for the spin-contaminated transition state TS_A, we performed qualitative RHF-RCCSD(T)/6-31+G(d) and UHF-UCCSD(T)/6-31+G(d) single-point energy calculations with the Gaussian 09 program on the wB97xd/aug-ccpVTZ - optimized geometry. While the UHF energy was 60.5 kcal mol⁻¹ below the RHF energy, the UHF-UCCSD energy was 344.0 kcal mol⁻¹ and the UHF-UCCSD(T) energy 272.9 kcal mol⁻¹ above the RHF-RCCSD and RHF-RCCSD(T) energies, respectively. Inspection of the CCSD iterations (over 300 were required for convergence) indicates that the UCCSD probably converged to the wrong state. A similar comparison for the alternative TS_A isomer, for which CCSD convergence problems did not occur, yielded more modest energy differences, but the UHF-UCCSD(T)

energy was still $5.3 \text{ kcal mol}^{-1}$ above the RHF-RCCSD(T) energy. Spin contamination at the UHF level was extreme for both of the TS_A isomers; $\langle S^2 \rangle = 0.93\text{...}0.95$ before and $0.19\text{...}0.20$ after annihilation. This indicates that using a UHF reference in the coupled cluster calculations would neither lower the barrier, nor improve the reliability of the results and suggests that multireference calculations are required to attain better accuracy. These problems are likely related to the difficulties of even advanced methods like CCSD(T) or even MRCISD in describing the structure and stability of the HO_3 intermediate product. Varandas (2012) has suggested that a quantitative prediction of the dissociation energy of HO_3 would require FCI calculations.

The DFT relative energies for reactant and products are within 4 kcal mol^{-1} of the ROHFROCCSD(T)-F12/VDZ-F12//wB97XD/aug-cc-pVTZ energies and give an idea of the uncertainty expected in these calculations. For the RI and the TS's the difference is higher than usual and, in conjunction with the spin and T1 values, an indication that multireference calculations are needed to obtain accurate values. The DFT barrier values for the ROOH and $\text{R}(\text{C}=\text{O})$ channels are such that these products would not be observed. The F12 barriers for these channels are lower and thus in better agreement with experiment.

The formation of intermediate product complexes of energies comparable to that of the reactants allow for back reactions that further complicate determination of yields.

B.5.4 Second Tetroxide

We have found a second tetroxide that also leads to both RO and $\text{R}(\text{C}=\text{O})$. It is lower in energy than the one in Figure B.6, however the TS leading to the products are higher in energy. These pathways are shown in Figure B.14 in the Supporting Information.

B.5.5 Decomposition of Alkoxy Radical Formed from External OH Addition to MVK (R1a)

The decomposition of the alkoxy radical formed in the reaction of NO with the peroxy radical produced in R1a can lead to either methylglyoxal ($\text{CH}_3(\text{C}=\text{O})\text{CHO}$) and the CH_2OH radical or glycolaldehyde (CH_2OHCHO) and the $\text{CH}_3\text{C}=\text{O}$ radical. The calculated energies and stationary points are shown in Figure B.15 and Table B.12 in the Supporting Information. The barrier of the internal alkoxy decomposition will likely be dominated by glycolaldehyde formation.

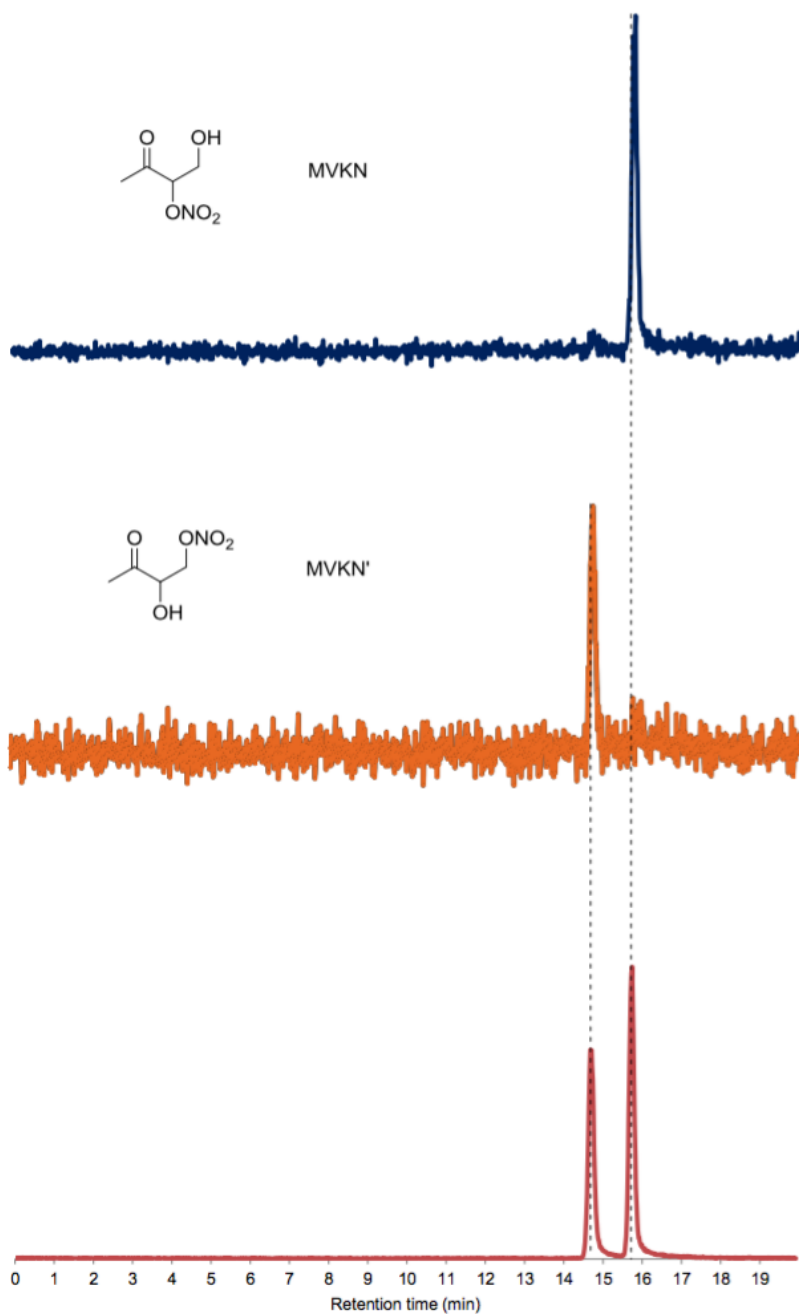


Figure B.9: Chromatographic analysis used for the identification of MVKN and MVKN'. Data are derived from experiments 8 (bottom panel), 14 (mid panel), and 12 (top panel). The latter two experiments isolated the chemistry of individual RO₂, enabling the structures and retention times of the individual organic nitrates to be discerned. This assignment also matches the elution order previously reported using a similar column (Lee *et al.*, 2014).

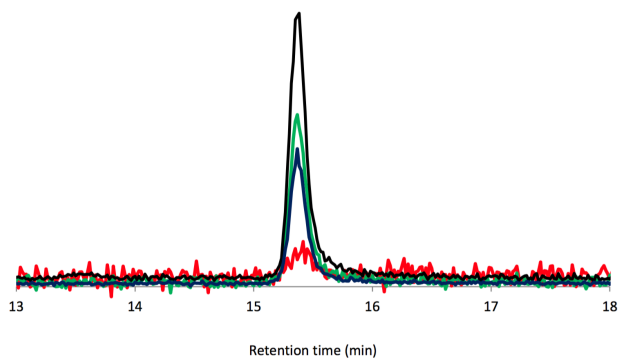


Figure B.10: Chromatographic analysis of the 4,3 hydroxy hydroperoxide derived from experiment 1. Shown are the major product ions in order of descending area: m/z 139 (black), m/z 101 (green), m/z 205 (blue), m/z 63 (red).

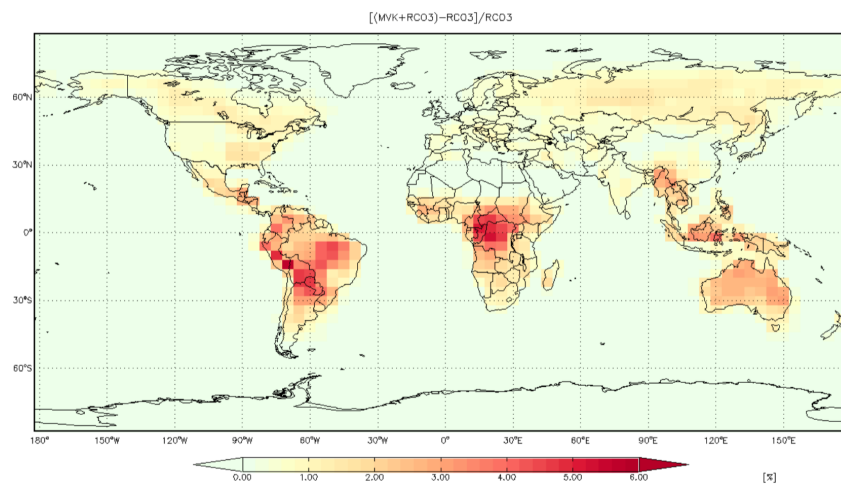


Figure B.11: Relative difference in the OH mixing ratio for MVK + RCO₃ in the boundary layer (0-1 km).

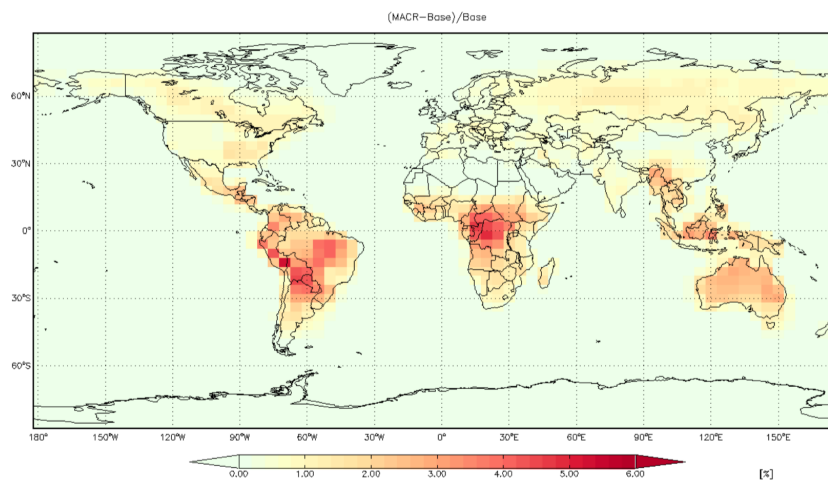


Figure B.12: Relative difference in the OH mixing ratio for MACR in the boundary layer (0-1 km).

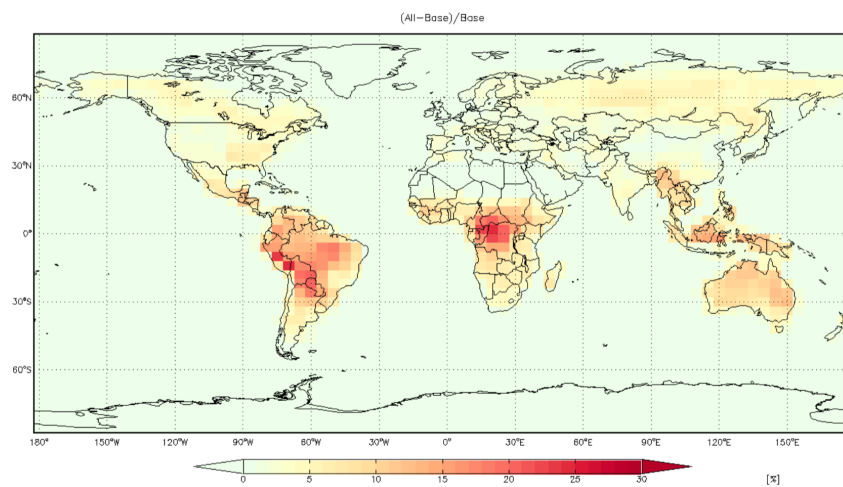


Figure B.13: All inclusive: MVK, MACR isomerization, RCO_3 , J_{ROOH} ; relative difference in the boundary layer (0-1 km).

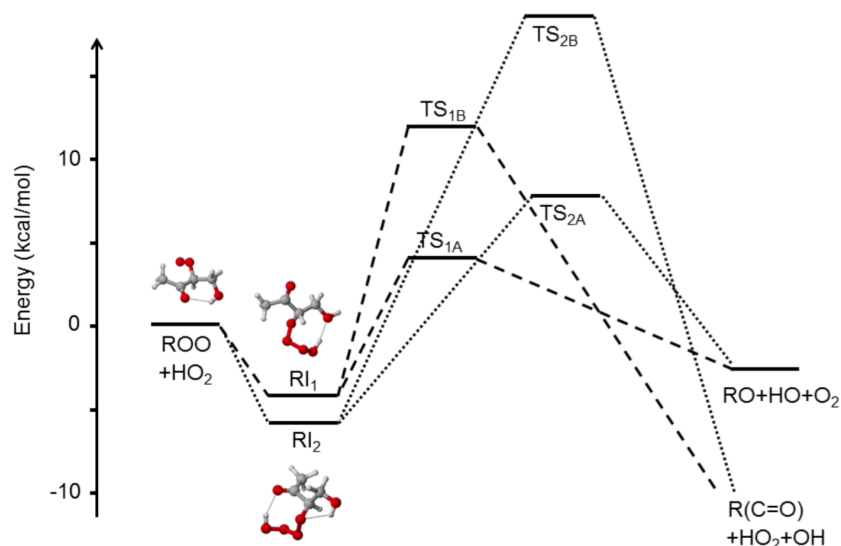


Figure B.14: Relative energies (ΔG_{298K}) for the two singlet $RO_2 + HO_2$ channels, including the second tetroxide (RI_2). RI_1 is identical to RI in the manuscript. We have used $wB97XD/aug-ccpVTZ$ thermochemistry with $ROHF-ROCCSD(T)-F12/VDZ-F12$ energies. The $wB97XD/auGCc-pVTZ$ geometries for each of the stationary points are shown.

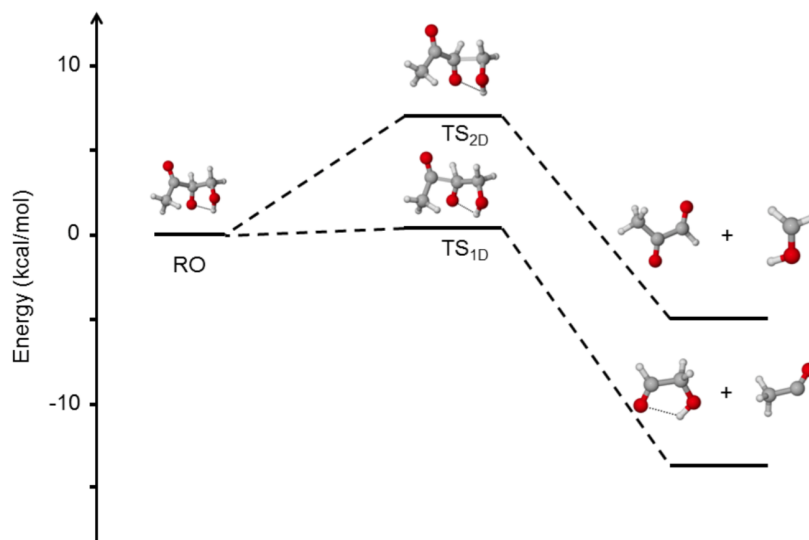


Figure B.15: Relative energies (ΔG_{298K}) for the two decomposition channels of the alkoxy formed from external OH addition to MVK . We have used $wB97XD/aug-cc-pVTZ$ thermochemistry with $ROHF-ROCCSD(T)-F12/VDZ-F12$ energies. The $wB97XD/aug-cc-pVTZ$ geometries for each of the stationary points are shown.

molecule	m/z	μ (D)	α (Å ³)	k_x (10^{-9} cm ³ molecule ⁻¹ s ⁻¹)	calculated sensitivity ($\times 10^{-4}$)	experimental sensitivity ($\times 10^{-4}$)
ISOPN-4,3	232	2.5	11	1.9	3.1	3.7
glycolaldehyde	145	2.3	4.5	2.0	3.1	3.0 ± 0.2
hydroxy diketone	187	2.1	7.2	1.8	2.7	-
4,3-hydroxyhydroperoxide	205+139+101+63	2.6	8.1	2.0	3.1	-
MVKN	234	2.3	9.9	1.8	2.8	2.6 ± 0.3
MVKN'	234	2.2	9.7	1.8	2.7	3.0 ± 0.3

Table B.6: Calculated conformer-weighted dipole moments (μ) and polarizabilities (α) served as the basis for sensitivity determination (see Paulot *et al.* (2009a) calculations for the hydroxy diketone and 4,3-hydroxy-hydroperoxide were performed in support of this work by HGK at the B3LYP/6-31G(d) level). k_x is the weighted average of the calculated collision rates (Su and Chesnavich, 1982) for conformers having an abundance greater than 5%. These are normalized to the average of the calculated collision rates for CF₃O⁻ with MVKN and MVKN' at 298 K ($k = 1.8 \times 10^{-9}$ cm³ molecule⁻¹ s⁻¹) and the mean of the experimentally determined MVKN and MVKN' sensitivities was used to infer the sensitivity for compounds for which no standards were available. Masses (m/z) represent the cluster mass with CF₃O⁻. For compounds reacting with CF₃O⁻ to form multiple product ions, the sum of all known product ions have been used for quantification. Isoprene nitrate (1-hydroxy-3-methylbut-3-en-2-yl nitrate, ISOPN-4,3) has been included for additional comparison between theory and experiment. Calculated and experimental sensitivities are in units of normalized counts pptv⁻¹ for the CF₃O⁻ CIMS. Hydroxy nitrate sensitivities were determined using thermal dissociation LED-induced fluorescence (Teng *et al.*, 2015) and glycolaldehyde was calibrated as described in the current work. Uncertainties are indicated for measured sensitivities.

scenario	base model	revised model
Base: VRO ₂ + NO →	0.88NO ₂ + 0.35HO ₂ + 0.35CH ₂ O + 0.53MCO ₃ + 0.53GLYC + 0.35MGLY + 0.12MVKN: k=2.7 × 10 ⁻¹² × e ^(350/T)	0.965NO ₂ + 0.249HO ₂ + 0.249CH ₂ O + 0.716MCO ₃ + 0.716GLYC + 0.249MGLY + 0.035MVKN: k=2.7 × 10 ⁻¹² × e ^(350/T)
MVK: VRO ₂ + HO ₂ →	1.000 VRP: k=1.82 × 10 ⁻¹³ × e ^(1300/T)	0.38VRP + 0.62OH + 0.37GLYC + 0.13MEK + 0.37MCO ₃ + 0.25HO ₂ + 0.12MGLY + 0.12CH ₂ O: k=1.82 × 10 ⁻¹³ × e ^(1300/T)
MVK + RCO ₃ : MCO ₃ + HO ₂ →	0.16ACTA + 0.16O ₃ + 0.61OH + 0.61MO ₂ + 0.23MAP: k=5.2 × 10 ⁻¹³ × e ^(980/T) ;	0.16ACTA + 0.16O ₃ + 0.61OH + 0.61MO ₂ + 0.23MAP: k=5.2 × 10 ⁻¹³ × e ^(980/T) ;
RCO ₃ + HO ₂ →	0.16RCOOH + 0.16O ₃ + 0.61OH + 0.61ETO ₂ + 0.23PP: k=4.3 × 10 ⁻¹³ × e ^(1040/T) ;	0.16RCOOH + 0.16O ₃ + 0.61OH + 0.61ETO ₂ + 0.23PP: k=4.3 × 10 ⁻¹³ × e ^(1040/T) ;
MAO ₃ + HO ₂ →	0.16O ₃ + 0.61OH + 0.61CO ₂ + 0.61CH ₂ O + 0.40MO ₂ + 0.4CO + 0.21MCO ₃ + 0.23MAOP: k=4.3 × 10 ⁻¹³ × e ^(1040/T) ;	0.16O ₃ + 0.61OH + 0.61CO ₂ + 0.61CH ₂ O + 0.40MO ₂ + 0.4CO + 0.21MCO ₃ + 0.23MAOP: k=4.3 × 10 ⁻¹³ × e ^(1040/T) ;
VRO ₂ + HO ₂ →	1.000VRP: k=1.82 × 10 ⁻¹³ × e ^(1300/T)	0.38VRP + 0.62OH + 0.37GLYC + 0.13MEK + 0.37MCO ₃ + 0.25HO ₂ + 0.12MGLY + 0.12CH ₂ O: k=1.82 × 10 ⁻¹³ × e ^(1300/T)
MACR MRO ₂ →	1.000CO + 1.000HAC + 1.000OH: k=0	1.000CO + 1.000HAC + 1.000OH: k=2.90 × 10 ⁷ × e ^(-5297/T)

Table B.7: Revisions incorporated into the GEOS-Chem mechanism. The scenarios are consistent with those described in Table B.5. The base scenario includes the alkyl nitrate branching determined in this work. Naming conventions used below can be found at <http://wiki.seas.harvard.edu/GEOS-Chem>.

lower-bound wavelength (nm)	upper-bound wavelength (nm)	base cross section (cm ²)	new cross section (cm ²)
289	298.25	5.621×10^{-21}	5.665×10^{-20}
298.25	307.45	3.573×10^{-21}	4.000×10^{-20}
307.45	312.45	2.441×10^{-21}	2.740×10^{-20}
312.45	320.30	1.755×10^{-21}	2.140×10^{-20}
320.30	345	7.405×10^{-22}	7.085×10^{-21}
345	412.45	4.261×10^{-23}	5.634×10^{-22}
412.45	850	0	0

Table B.8: Revised wavelength bins utilized to define the photolysis frequency of the MVK hydroperoxide in the model.

	$\langle S^2 \rangle$ before annihilation	$\langle S^2 \rangle$ after annihilation	T1
ROO	0.7546	0.7500	0.023
OOH	0.7543	0.7500	0.034
³ TS	2.0124	2.0001	0.032
ROOH	0.0	0.0	0.013
O ₂	2.0101	2.0001	0.008
RI	0.0	0.0	0.016
¹ TS _A	0.5729	0.0167	0.020
RO	0.7577	0.7500	0.028
OH	0.7529	0.7500	0.007
¹ TS _B	0.0	0.0	0.021
R(C=O)	0.0	0.0	0.014

Table B.9: Spin contamination and T1 diagnostic in the calculations from the different RO₂ + HO₂ channels. $\langle S^2 \rangle$ are from the UwB97XD/aug-cc-pVTZ calculation, and T1 is from the ROHF-ROCCSD(T)-F12/VDZ-F12//wB97XD/aug-cc-pVTZ calculation.

	ΔE^a	ΔE^b	ΔG_{298K}^c	TS (imaginary frequency, cm^{-1})
ROO + HO ₂	0.0	0.0	0.0	-
RI \equiv RI ₁	-12.2	-20.4	-4.1	-
RI ₂	-13.7	-21.7	-6.0	-
TS _{1A} \equiv TS _A	+2.5	-8.3	+4.1	212i
TS _{2A}	+3.9	-5.1	+7.8	169i
TS _{1B} \equiv TS _B	+11.2	-0.7	+12.0	905i
TS _{2B}	+18.1	+6.7	+18.9	1011i

Table B.10: Comparison of the energetics of the channels associated with the two different tetroxides. Energies are in units of kcal mol^{-1} and are calculated with ^awB97XD/aug-cc-pVTZ, ^bROHF-ROCCSD(T)-F12/VDZ-F12//wB97XD/aug-cc-pVTZ, or ^cthe wB97XD/aug-cc-pVTZ thermochemistry with CCSD(T)-F12/VDZ-F12 single point energy correction.

	$\langle S^2 \rangle$ before annihilation	$\langle S^2 \rangle$ after annihilation	T1b
RI ₂	0.0	0.0	0.016
TS _{2A}	0.6813	0.0250	0.021
TS _{2B}	0.0	0.0	0.022

Table B.11: Spin contamination and T1 diagnostic associated with the second tetroxide RI₂ and its TS. $\langle S^2 \rangle$ are from the UwB97XD/aug-cc-pVTZ calculation, and T1 is from the ROHF-ROCCSD(T)-F12/VDZ-F12//wB97XD/aug-cc-pVTZ calculation.

	ΔE^a	ΔE^b	ΔG_{298K}^c	TS (imaginary freq., cm^{-1})
RO	0.0	0.0	0.0	-
TS _{1D}	+3.3	+1.5	+0.4	199.4i
GLYC + CH ₃ (C=O)	+14.2	+10.5	-5.1	-
TS _{2D}	+9.0	+8.2	+6.9	237.6i
MGLY + CH ₂ OH	+3.9	+0.2	-14.2	-

Table B.12: Energetics of the different RO decomposition channels. Energies are in units of kcal mol^{-1} and are calculated with ^awB97XD/aug-cc-pVTZ, ^bROHF-ROCCSD(T)-F12/VDZ-F12//wB97XD/aug-cc-pVTZ, or ^cthe wB97XD/aug-cc-pVTZ thermochemistry with CCSD(T)-F12/VDZ-F12 single point energy correction. For TS_{1D}, the structure is optimized and frequencies and thermal contributions to ΔG_{298K} calculated using tight optimization criteria and an ultrafine integration grid in order to remove a spurious near-zero imaginary frequency. For consistency, the DFT energy has been computed with a single-point energy evaluation using the normal integration grid.

	$\langle S^2 \rangle$ before annihilation	$\langle S^2 \rangle$ after annihilation	T1b
TS _{1D}	0.7617	0.7500	0.018
CH ₃ (C=O)CHO	0.0	0.0	0.014
CH ₂ OH	0.7534	0.7500	0.020
TS _{2D}	0.7650	0.7501	0.018
CH ₂ OHCHO	0.0	0.0	0.015
CH ₃ (C=O)	0.7542	0.7500	0.016

Table B.13: Spin contamination and T1 diagnostic associated with the second RI and its TS. $\langle S^2 \rangle$ are from the UWB97XD/aug-cc-pVTZ calculation, and T1 is from the ROHF-ROCCSD(T)-F12/VDZ-F12//wB97XD/aug-cc-pVTZ calculation.